International Journal of Solids and Structures 257 (2022) 111806

Contents lists available at ScienceDirect

International Journal of Solids and Structures

journal homepage: www.elsevier.com/locate/ijsolstr

Probing the stability of thin-shell space structures under bending

Fabien Royer [a,1], John W. Hutchinson [b], Sergio Pellegrino [a,*]

[a] Graduate Aerospace Laboratories, California Institute of Technology, 1200 E California Blvd., Pasadena, CA 91125, USA
[b] John A. Paulson School of Engineering and Applied Sciences, Harvard University, 29 Oxford St, Cambridge, MA 02138, USA

ARTICLE INFO

Keywords:
Thin shells
Buckling
Stability
Buckling localization
Probing

ABSTRACT

The stability of lightweight space structures composed of longitudinal thin-shell elements connected transversely by thin rods is investigated, extending recent work on the stability of cylindrical and spherical shells. The role of localization in the buckling of these structures is investigated and early transitions into the post-buckling regime are unveiled using a probe that locally displaces the structure. Multiple probe locations are studied and the probe force versus probe displacement curves are analyzed and plotted to assess the structure's stability. The probing method enables the computation of the energy input needed to transition early into a post-buckling state, which is central to determining the critical buckling mechanism for the structure. A stability landscape is finally plotted for the critical buckling mechanism. It gives insight into the post-buckling stability of the structure and the existence of localized post-buckling states in the close vicinity of the fundamental equilibrium path.

1. Introduction

Thin-shell structures are used extensively in engineering applications. In the aerospace sector, they are a key enabler of lightweight air and space vehicles. While the use of thin-shell structures dramatically reduces the structural mass, their mode of failure is often governed by buckling, which is hard to predict. Buckling of thin-shell structures is characterized by a sub-critical bifurcation, which means that the structure exhibits a falling unstable post-buckling path right after the bifurcation point is reached. This sudden drop in load-carrying capabilities leads to a dramatic collapse if the post-buckling path never regains stability. Buckling is to be avoided at all cost in these cases. However, in recent adaptive structures and materials, buckling is no longer seen as failure but as a key shape-changing mechanism, which enables switching among multiple functional configurations (Hu and Burgueño, 2015; Medina et al., 2020). Whether buckling is used or to be avoided, understanding its cause and predicting its occurrence is crucial, and this has been the subject of numerous research studies over the past one hundred years.

From the early 1920s, many shell buckling experiments were conducted, and experimental buckling loads were consistently observed to be lower than linearized classical buckling predictions. This discrepancy was later linked to the presence of initial imperfections in the shell geometry (Von Karman and Tsien, 1941; Donnell and Wan, 1950; Koiter, 1945). Indeed, for sub-critical bifurcations, there exists a range of loading for which the structure's fundamental (unbuckled) state is meta-stable, which makes the transition into post-buckling extremely sensitive to imperfections and disturbances. On the upside, this can also offer opportunities to build complex meta-stable structures (Zareei et al., 2020) by using buckled thin-shells as the main building blocks. In order to deal with the extremely sensitive buckling behavior in engineering applications, the design process relies heavily on buckling knockdown factors applied to the classical buckling load. Determining the adequate knockdown factor, unique for each structure/load combination, is of utter importance. It led to the NASA space vehicle design criteria for the buckling of thin-walled circular cylinders (NASA, 1965). These criteria, widely seen as very conservative, have been revisited by NASA's Shell Buckling Knockdown Factor (SBKF) Project, which has focused on testing shells with known imperfections and non-uniformities in loading and boundary conditions (Hilburger, 2012). It has been shown that knowing accurately the structure's initial geometry enables the accurate prediction of the buckling event (Lee et al., 2016). However, in many applications, measuring the shape of the structure before use can be both expensive and in some cases impossible, and the traditional buckling and post-buckling predictions rely on seeding a linear combination of the first buckling modes as imperfections (Riks, 1979; Rahman and Jansen, 2010).

Another complication arising from unstable bifurcations is the localization of buckling deformations. This is observed for instance for beams on an elastic foundation (Wadee et al., 1997) and more importantly for thin-shell structures such as the compressed cylindrical

* Corresponding author.
E-mail address: sergiop@caltech.edu (S. Pellegrino).
[1] Currently at: Department of Aeronautics and Astronautics, Massachusetts Institute of Technology, Cambridge MA 02139-4307, USA.

https://doi.org/10.1016/j.ijsolstr.2022.111806
Received 21 December 2021; Received in revised form 9 May 2022; Accepted 13 June 2022
Available online 17 June 2022

shell (Hunt and Neto, 1991) as well as the spherical shell under pressure (Hutchinson, 2016). The nature of localization itself generates a large number of post-buckling solutions even for a small set of classical buckling modes, since the deformations can localize at many different locations on the structure. This is referred to as spatial chaos (Thompson and Virgin, 1988). Localization can arise on post-buckling branches determined by the buckling modes, as observed in the spherical shell under pressure (Audoly and Hutchinson, 2020; Hutchinson and Thompson, 2017a). In addition, localization can also appear on post-buckling paths disconnected from the fundamental path while running asymptotically close to it (Groh and Pirrera, 2019). In both cases, localized buckling can be triggered earlier than the first buckling load if a small amount of energy is input into the structure. It has been shown, for the compressed cylindrical shell, that a single localized dimple forming in the middle of the structure constitutes the lowest escape into buckling (Horák et al., 2006) and may therefore be the critical buckling mechanism. This mode is not a bifurcation per se, but rather a mode "broken away" from the fundamental path. The single dimple state sits on a ridge in the total energy of the system between the pre-buckling well and the local post-buckling well and corresponds to the lowest mountain pass between these two states in the energy landscape (Horák et al., 2006). For the cylinder, the single dimple can evolve to more and more complex post-buckling deformations through a series of destabilizations and restabilizations, until the cylinder is fully populated by dimples (Kreilos and Schneider, 2017; Groh and Pirrera, 2019). This process is called snaking and adds additional complexity to the full post-buckling sequence resolution.

For all of the reasons mentioned above, predicting buckling is extremely difficult for shell structures and often relies on a case by case approach. Recent work has focused on the sensitivity of the buckling phenomenon to disturbances in thin cylindrical and spherical shells. A non-destructive experimental method, first proposed in 2015 to study the meta-stability of the fundamental path, focuses on determining the energy barrier separating the fundamental path and critical localized post-buckling states (Thompson, 2015; Thompson and Sieber, 2016; Hutchinson and Thompson, 2017b). The search for the critical buckling mechanism is carried out by imposing a local radial displacement in the middle of the structure using a probe. This method effectively quantifies the resistance of a shell buckling in the single dimple mode mentioned earlier. The method has been successfully applied to cylindrical shells (Virot et al., 2017) and pressurized hemispherical shells (Marthelot et al., 2017). These experiments quantified in particular the onset of meta-stability, often referred to as "shock sensitivity" (Thompson and van der Heijden, 2014) and a comparison with historical test data has shown that this specific loading can serve as an accurate lower bound for experimental buckling loads (Groh and Pirrera, 2019; Gerasimidis et al., 2018).

More recent work has investigated the interaction between probing and geometric defects in cylindrical (Yadav et al., 2021) and spherical shells (Abbasi et al., 2021). These experiments showed that a specific probing strategy, called ridge tracking (Abramian et al., 2020), enables the non-destructive determination of the actual buckling load of an imperfect shell. Probing in the immediate vicinity of the dominant imperfection is required. Finally, a similar probing methodology has been applied to circular arches (Shen et al., 2021a), cylindrical shell roofs (Shen et al., 2021b), and prestressed stayed columns (Shen et al., 2022), and the use of multiple probes has enabled the exploration of the complete unstable behavior of these structures, beyond limit and branching points.

The present paper applies these recent breakthroughs to more complex thin-shell structures, and is inspired by recently proposed spacecraft structures that use thin-shell components to build large space systems. In particular, modular structural architectures for ultralight, coilable space structures suitable for large, deployable, flat spacecraft (Goel et al., 2017; Arya et al., 2016) are being investigated in the Space-based Solar Power Project (SSPP) at Caltech. In the deployed configuration, each spacecraft measures up to 60 m × 60 m in size and is loaded by solar pressure. The main building block is a ladder-type structure made of two triangular rollable and collapsible (TRAC) longerons (Murphey and Banik, 2011), connected transversely by rods (battens). Scaled laboratory prototypes of this structure have been built (Gdoutos et al., 2020, 2019), and analysis has shown that local buckling plays a key role in its behavior (Royer and Pellegrino, 2020). The size of the structure, together with the complexity of its components and the distributed nature of the loading, would make it very challenging to conduct experimental studies.

In order to address these limitations, a simpler structure is proposed in the present paper and its behavior under pure bending is studied. This structure, shown in Fig. 1, is made of longerons and battens like the SSPP structures, but the longeron's complex original cross-section has been replaced by a circular-arc cross-section. While this structure and loading are different from the specific structures of interest for the above-described space application, it enables us to draw general conclusions on the buckling of space structures with thin-shell open cross-sections. The computational analysis presented here investigates the buckling behavior of such a structure and assesses if and when early transitions into post-buckling can occur, using the novel probing methodology. It also serves as a proof of concept for the experimental study in Royer (2021).

The paper is structured as follows. Section 2 describes in more detail the structure and the problem. Following a classical buckling analysis, Section 3 highlights the importance of localization and spatial chaos and justifies the use of the newly-introduced probing methodology. In Section 4, probing is applied along the entire structure to determine the location at which local buckling can appear, and a critical probing scheme is identified. The analysis is then generalized in Section 5 to more complex probing scenarios exhibiting instabilities, and leads to an energy map from which the critical buckling mechanism is identified. Finally a stability landscape of shell buckling is computed in Section 6 to highlight key characteristics of the critical buckling mechanism. It shows qualitative agreement with landscapes previously constructed for cylindrical and spherical shells, and for ladder-type structures containing TRAC longerons (Royer and Pellegrino, 2020, 2022).

2. Computational model of strip structure

2.1. Geometry and material properties

The analysis presented in this paper is restricted to the single geometry shown in Fig. 1. The dimensions were chosen on the basis of a future experiment that will use an existing experimental apparatus.

The structure, referred as a strip, is composed of two thin-shell longerons of length 0.4 m and with circular-arc cross section. The opening angle is 60 deg, the arc radius is 10 mm, and the shell thickness is 0.1 mm, which correspond to a bending stiffness comparable to the SSPP structures. The two longerons are connected by six regularly spaced transverse circular rods called battens. The batten spacing is 80 mm, which ensures that several battens connecting the two longerons. The batten length is 50 mm, and the batten cross-section radius is 1 mm.

A finite element model of the structure is built using the Abaqus 2019 commercial software. The longerons are modeled with 4-node reduced integration shell elements (S4R) and the battens with linear 3D beam elements (B31). An isotropic material with Young's modulus $E = 130$ GPa, and Poisson's ratio $\nu = 0.35$ is considered for both battens and longerons.

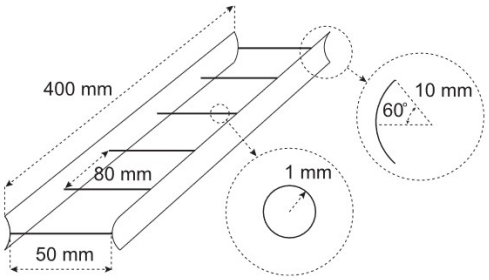

Fig. 1. Strip structure composed of two thin-shell longerons connected by battens.

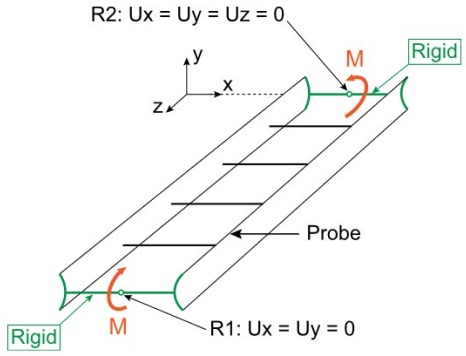

Fig. 2. Schematic representation of finite element model. The end battens and cross-sections (green) are undeformable. R1 is allowed to translate along the z-axis and to rotate along all 3 axes, R2 is pinned and is free to rotate. Two equal and opposite moments are applied at the reference points. For a probing simulation (Section 4), a probe is applied to the top edge of the longeron (longeron and z location determined by probing scheme). It consists in an applied displacement on the probe node directed along the x-axis.

2.2. Finite element analysis

The end battens and the longeron end cross-sections are made undeformable and fully coupled to reference points R1 and R2, as shown in Fig. 2. The boundary conditions and loading are applied to these reference points. The structure is simply supported at both ends: one reference point is pinned (all translations blocked) at one end while the z-translation is allowed for the reference point at the other end. Two equal and opposite moments of magnitude M are applied at the reference points, and an arc-length solver (Riks solver in Abaqus standard) is used to statically deform the structure and extract the overall moment/rotation curve. In addition, in Section 4, for each value of the moment, the top edge of the longeron will be probed by applying a transverse nodal displacement U_x at location z, and the probe reaction force will be extracted. The two control parameters in these calculations are thus the end moment and the probe displacement.

This strip structure has nonlinear pre-buckling behavior, meaning that the computed buckling eigenmodes change as the structure approaches the buckling limit. This type of nonlinearity was previously reported for thin shell structures (Leclerc and Pellegrino, 2020). Hence, we will need to distinguish between two types of bifurcation buckling analyses and their associated modes. We will use the standard terminology, classical buckling loads and modes, for results in which the pre-buckling state used in the eigenvalue analysis has been linearized, either about the condition at zero load or at a non-zero load. Our approach will be making use of these eigenloads and eigenmodes to gain insight into the buckling behavior of the strip. However, most references to buckling load and modes throughout the paper will be to "exact" buckling loads and modes computed by analyzing the bifurcation from the nonlinear pre-buckling state. We will mostly refer to the "exact" analysis and its outcome with the brief terminology: buckling analysis, buckling loads, and buckling modes. However, if there is any ambiguity the additional terminology, linearized or nonlinear pre-buckling state, will be appended.

3. Localization and spatial chaos

3.1. Buckling modes and limit points

The first step in assessing the buckling behavior of the strip is to carry out a classical eigenvalue analysis to determine a sequence of the applied moments and associated modes at which buckling bifurcations from the perfect strip occur. This information gives a picture of not only the lowest buckling load and associated mode but also of the bifurcation modes lurking above the lowest critical mode. Such information gives insight into potentially important imperfection shapes and to "nearby paths" which might play a role in the post-buckling behavior.

The computation of the "exact" bifurcation moments and modes is itself an iterative procedure because the pre-buckling behavior is nonlinear. To obtain first estimates of the bifurcation points, the pre-buckling nonlinearity is neglected using the ground-state linearity to compute a sequence of the lowest bifurcation eigenvalues (ABAQUS and other structural codes have options for making such eigenvalue evaluations). These bifurcation estimates are then used to guide the search for the bifurcations computed accounting for nonlinear pre-buckling behavior. With the full pre-buckling nonlinearity accounted for, the strip is then loaded by a moment below the first eigenvalue, the nonlinear pre-buckling problem is solved, and new estimates of the sequence of bifurcation points are computed by linearizing about that state. This iterative process is repeated with an increasing applied moment in each iteration until the bifurcation moments converge. For the strip, nine bifurcation points are determined in the loading interval before the strip attains a limit moment on the fundamental pre-buckling path. As noted earlier, to distinguish between a buckling load of the perfect strip computed using ground state linearity (traditionally called a "classical buckling load") and the buckling load computed accounting for pre-buckling nonlinearity, we will briefly refer to the latter as the "buckling load" and is associated eigenmode as the "buckling mode". The results of this analysis are shown in Fig. 3.

Both a classical Newton–Raphson solver and the Riks solver are used to trace the response of the structure in its unbuckled configuration. The Riks method uses the load magnitude as an additional unknown and solves simultaneously for loads and displacements. The simulation progresses by incrementing the arc-length along the static equilibrium path in load–displacement space, enabling the resolution of unstable responses. The Newton–Raphson solver reaches a limit point at $M = 1464.2$ N mm, while the Riks solver bifurcates from the fundamental path to a secondary branch at $M = 1435$ N mm. Note that this moment magnitude is between the first and second buckling moments in Fig. 3.

3.2. Localization and post-buckling paths

We wish to trace the post-buckling paths corresponding to several of the lowest buckling eigenmoments and study the evolution of the structure's shape along these paths. Of primary interest is the moment/rotation relation for the strip when equal and opposite moments are applied at the strip ends and the rotation corresponds to the rotation around the x-axis of the end located at $z = 0$ (c.f., Fig. 2).

As a first step, a standard method is used to trace the post-buckling paths associated with the first three buckling modes as described next. Each mode is seeded in the structure's initial geometry as a geometric imperfection. The maximum amplitude of this initial imperfection is taken between 1% and 10% of the shell thickness, t. The Riks solver is used to trace the post-buckling response of the imperfect structure.

The computed paths are shown in Fig. 4, and the corresponding deformed shapes are shown in Fig. 5. For the second buckling

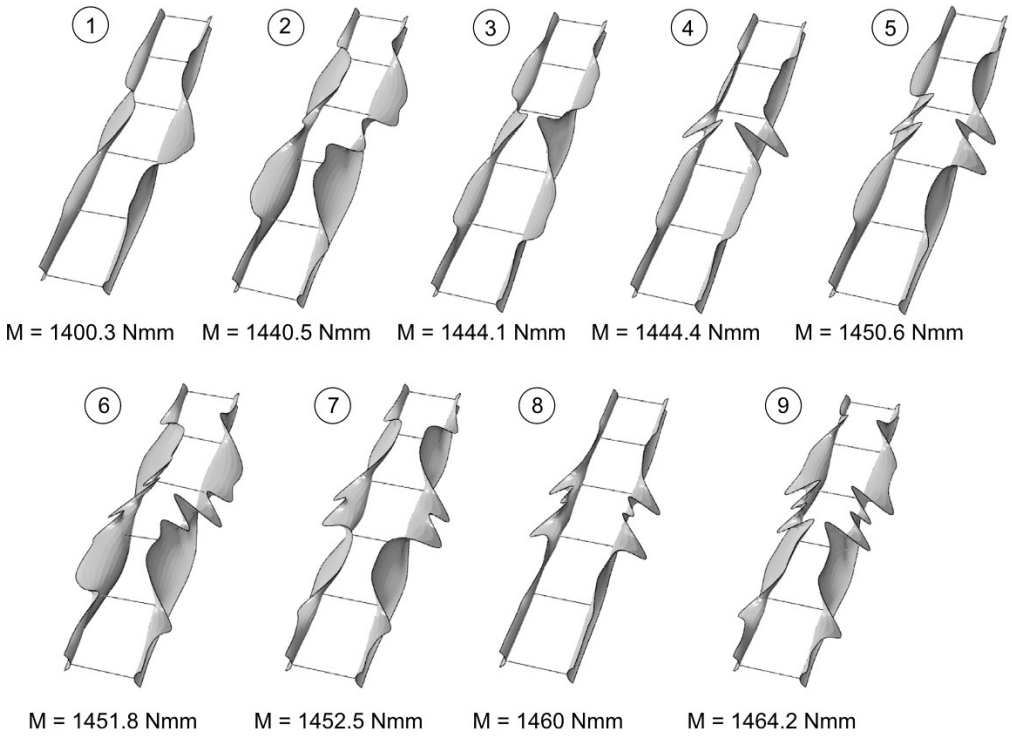

Fig. 3. Nine buckling modes with associated buckling moments found on the strip fundamental path. For each mode, the deformations of both longerons are concentrated along the longerons' top edge (edge in compression). These deformations involve both inward (towards the strip center) and outward displacements. The battens do not exhibit any appreciable deformation.

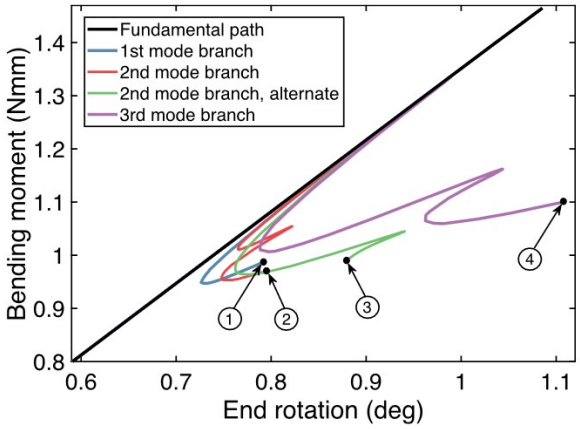

Fig. 4. Moment vs. rotation curves for the strip. The fundamental path (black) stops at the limit point $M = 1464.2$ N mm. The first buckling mode branch (blue) is obtained by seeding the first mode as imperfection with an amplitude of $8\%t$. The second branch (red) is obtained for the second mode imperfection with an amplitude of $8\%t$. The alternate second branch (green) is obtained for the second mode imperfection with an amplitude of $10\%t$. The third branch (purple) is obtained for the third mode imperfection with an amplitude of $8\%t$.

mode, two imperfection amplitudes have been used, yielding the two post-buckling paths shown.

The main observation is that, contrary to the bifurcation buckling modes, the deformed shapes for all the paths exhibit highly localized deformations. For the first and second mode branches, the post-buckling shapes are quite different from the initial imperfection. These shapes only exhibit inward buckling deformations, whereas the buckling modes also exhibit outward deformations. For the second mode branch, even a slight variation in imperfection amplitude changes the buckling location. For the second mode and third mode, the post-buckling paths undergo destabilization and restabilization. This phenomenon is referred to as homoclinic snaking and is also observed in axially compressed cylindrical shells (Groh and Pirrera, 2019). It physically corresponds to the sequential formation of buckles leading to a fully buckled shell. Snaking may occur also in the remaining localized paths if the analysis is pushed further. It is interesting to note that it was possible to resolve the post-buckling path for the third buckling mode without seeding any imperfection in the initial geometry.

For mode 1 and mode 2, the localization process initiates on the imperfect structure's fundamental path, before reaching the falling unstable post-buckling path. The initial deformation grows proportionally to the initial imperfection and then is followed by a transition to a localized mode shape before attaining a limit point. At this point, the location of maximum deformation has already been determined and, on the falling unstable path, the local deformation increases in amplitude without changing location. It is important to emphasize that the limit point for the imperfect structure is offset from the perfect structure's fundamental path, although extremely close to it, due to the eroding effect of the imperfection on the initial stiffness. In addition, these limit points appear at values of applied moment lower than the first buckling moment which reveals the structure's imperfection-sensitive nature.

Fig. 6 highlights the localization process for each of the first two buckling modes. The displacement of the longeron top edge in the $x - z$ plane is plotted at the limit point, as well as at the first post-buckling restabilization point and at the end of the post-buckling path. The normalized buckling mode of the perfect strip is also reported as a dashed line, for comparison.

For mode 1, localization occurs on two levels. At the structure's scale, local deformations only arise in longeron 1, while for longeron 2, the global deformation tends to cancel the undulations associated with the initial imperfection away for the point of localization. At the longeron scale, the deformed shape goes from a smooth hill to a sharp peak for longeron 2.

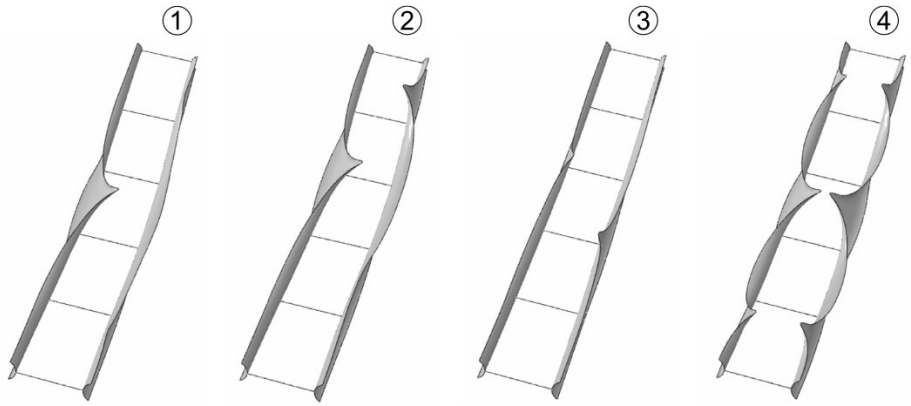

Fig. 5. Deformed shapes with magnification of 15X, obtained at the end of the four post-buckling paths of Fig. 4. They consist in localized longeron deformations and differ from the previously computed buckling modes. All deformations are inward, and the localization location differs between longerons for the mode 1 branch (labeled 1) and mode 2 branch (labeled 2).

In addition, the localization process is not unique. Different localization mechanisms are observed for buckling mode 2, depending on the imperfection amplitude, as seen in the deformed shape comparison of Fig. 5. The localization of mode 2 for an imperfection amplitude of 8%t is shown in Fig. 6c–d. It highlights the sequential formation of the longeron 1 and longeron 2 buckle, characteristic of the snaking process. In the case of buckling mode 3, the buckling mode shape is relatively localized and resembles the shape observed in Fig. 5 for the two central buckles. Therefore, no further localization is observed on the post-buckling path before the snaking process is triggered, and four highly localized buckles are formed closer to the longeron ends.

To conclude this section, we re-emphasize that multiple post-buckling paths have been shown to have initially unstable behavior, and in some cases the paths re-stabilized at lower loads. Four different imperfections based on the first three buckling modes have been considered here; other imperfections or linear combinations of buckling modes would give rise to different paths. Seeding different imperfections has highlighted qualitatively the importance of localization for this thin-shell structure and the fact its deformation can easily localize at many different locations. This multiplicity of buckling and post-buckling solutions is referred to as "spatial chaos". However, not all possible localized paths have been considered, and hence it is not known which path constitutes the easiest escape into post-buckling. Based on these qualitative observations, the next section searches for the critical localized path using the probing methodology introduced.

4. Probing along the strip length

4.1. Probing methodology

The previous section has shown that buckling localization can lead to a large number of post-buckling paths. Hence, the focus in the rest of this paper is on finding the critical buckling mechanism. Here "critical" means finding the easiest way the structure can buckle or, in other words, finding how early the transition into buckling can occur and which deformed shape is most likely to arise.

Two situations may be encountered when end-moments are applied on a strip. The first corresponds to an early transition to a path that intersects the fundamental path, and for which the deformation matches one of the buckling modes (at least at the bifurcation point). This situation may arise for buckling mode 3, for which no imperfection is needed to resolve the post-buckling path. The second situation corresponds to a transition to a disconnected equilibrium path, running in close vicinity of the fundamental path but without intersecting it (Hunt and Neto, 1991). In both cases, a finite input of energy into the system is required to make the structure transition early to a secondary equilibrium path. Note that here, "early transition" means that the transition to post-buckling occurs before reaching the first buckling moment. A key assumption made here is that the critical buckling mechanism will exhibit highly localized deformations. This is generally the case for thin-shell structures for which buckling is a sub-critical bifurcation and is motivated by the observations made in the previous section.

The probing method, which uses a probe that displaces the structure locally, is used to quantify the amount of disturbance needed to trigger early localized buckling. In this paper, the probing method is explored numerically and consists in applying a displacement directed along the x-axis to a node on the top edge of the longeron (the probed node), as illustrated in Fig. 2. The top edge is chosen because it corresponds to the location of the largest compressive stress when bending moments are applied to the structure.

The analysis goes as follows. Two end moments are applied on the perfect structure. When the desired moment magnitude is reached, the moment is kept constant and the probe displacement is increased. During probing, the probe reaction force is computed. This process is repeated for a range of moments, up to the first buckling moment, and for various probe locations along the longeron's top edge. The Abaqus static general solver (Newton–Raphson) is used for both the bending and probing steps. The analysis presented in this section is restricted to probing paths for which the probe displacement is monotonic.

Two features are of particular interest. The first corresponds to the range of applied moments for which buckled equilibrium states exist. An equilibrium state is found when the probe reaction force falls to zero. When such a situation is encountered, there exist at least two equilibrium configurations for a given moment and therefore the fundamental path is meta-stable. Above the moment for which negative probe forces are first encountered, a disturbance may trigger early buckling. The second important feature is the critical amount of energy that needs to be provided to the system to reach the buckled equilibria. It indicates the level of disturbance needed for the structure to transition early into these states.

Inspired by the types of deformations seen in the buckling modes, and restricting the study to at most a single probe per longeron, five probing schemes have been investigated: double outward probing, double inward probing, alternate probing, single outward probing, and single inward probing, as illustrated in Fig. 7. These probing schemes were chosen such that it would be possible to trigger the localized buckling modes of Fig. 5.

By characterizing the onset of meta-stability and the critical probe work needed to trigger buckling, we will be using probing as an efficient tool to navigate through the spatial chaos and to find the structure's critical buckling mechanism.

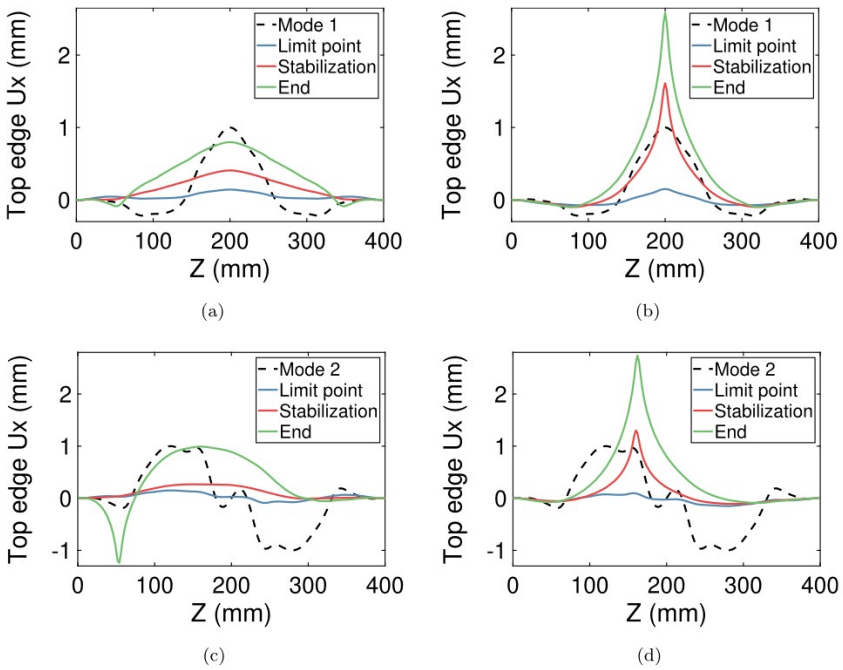

Fig. 6. (a–b) Localization process for (a) longeron 1 and (b) longeron 2, on the first mode post-buckling path, for an imperfection amplitude of 8%t. The longeron top edge displacement in the x-direction is plotted as a function of the z location. The normalized buckling mode is shown as a dashed line. The evolution of the longeron top edge deformation is reported at the limit point, where the post-buckling path first stabilizes, and at the end of the post-buckling path. (c–d) Localization process on the second mode post-buckling path, for an imperfection amplitude of 8%t for (c) longeron 1 and (d) longeron 2.

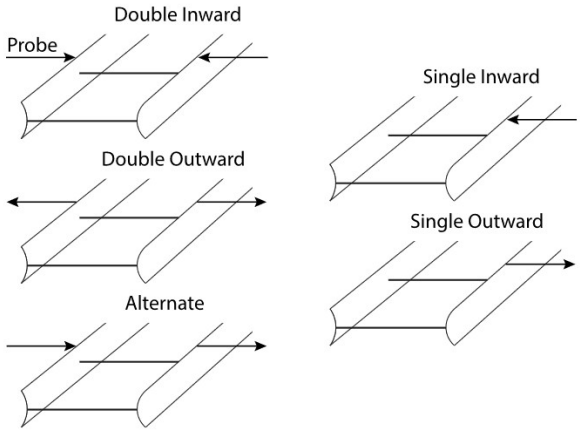

Fig. 7. Five probing schemes considered in this paper, with arrows representing the transverse probe displacement.

4.2. Double inward probing scheme

The double inward probing scheme is considered first. In this case, convergence is hard to achieve for probing with applied moments of around $M = 1100$ N mm, because instabilities are encountered. These instabilities are analyzed in detail in the next section.

For moments under 1000 N mm, the probing forces remain positive and the contours of constant probe force exhibit local extrema in the probe location/displacement plane. The probe force for two values of the moment has been plotted in Fig. 8 as a function of the probe location along the longeron edge (z-axis) and of the probe displacement. Fig. 8a shows the probing map for $M = 800$ N mm. The probe force is shown as a function of the probe displacement along the x-axis (U_x) and the probe location along the top of the longeron (x-axis). For ease of visualization, the regions corresponding to probe locations between 0 mm and 50 mm as well as between 350 mm and 400 mm are not shown since they exhibit large probe forces. In these two regions, the probe force vs. probe displacement curve is almost linear. For all other probe locations, the probe force increases monotonically as the probe displacement increases. However, the map exhibits many features, such as regularly spaced local minima of probe force for a given probe displacement. The lowest local minimum is attained in the middle of the structure (200 mm). The probe force is positive for all values of probe displacement. Fig. 8(b) shows the probing map for $M = 1040$ N mm. For probe locations ranging from 0 mm to 60 mm and from 340 mm to 40 mm, the probe force increases monotonically as the probe displacement increases. For all other probe locations, the probe force increases and then decreases. Regularly spaced local minima of probe force appear, and negative values are reached in the middle (200 mm). The spacing between local minima corresponds to the batten spacing.

In fact, additional simulations showed that the probe force at the center first falls to zero for $M = 1015.5$ N mm. This critical load corresponds to the onset of meta-stability, at which early transition into buckling becomes possible. Based on the probing scheme, the associated post-buckling shape consists of an inward local buckle in the middle of each longeron. This shape resembles the third non-linear buckling mode found in Section 3.1.

4.3. Single inward probing scheme

The single inward probing scheme is considered next. The probing maps for four values of the applied moment are shown in Fig. 9.

Fig. 9a shows the probing map for $M = 800$ N mm. As the probe displacement increases, the probe force increases monotonically, except near the middle, where a basin of local minima appears (probe displacement of 1.2 mm). The probe force is positive everywhere.

Fig. 9b shows the probing map for $M = 1040$ N mm. Local maxima of probe force appear and form a hill separating the fundamental path from regions with local minima. The local minima are negative near the middle of the strip, whereas at other locations they are positive, although very close to zero. This map resembles the map obtained for the double inward probing scheme.

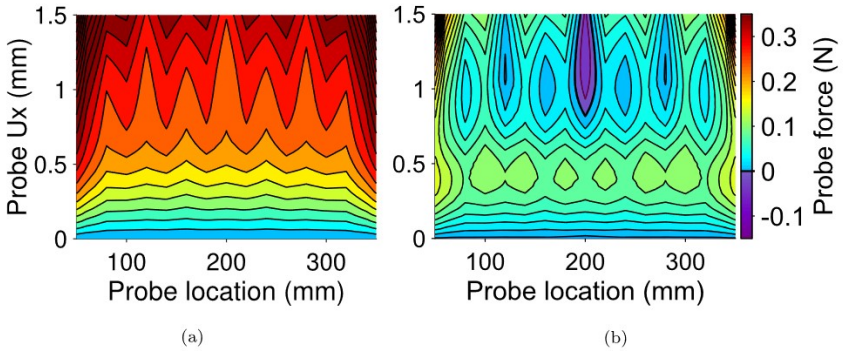

Fig. 8. Double inward probing map for (a) $M = 800$ N mm and (b) $M = 1040$ N mm. The spacing between contours is 0.05 N.

Fig. 9c shows the probing map for $M = 1200$ N mm, which resembles qualitatively Fig. 9b. A local minimum of probe force appears for a probe displacement of 0.2 mm, before reaching a second minimum at 0.35 mm, at the center of a region of negative probe forces. However, when probing at locations other than the middle, the probing path encounters instabilities as the probe force decreases after the peak, and the Newton–Raphson solver aborts. It leaves the probing map incomplete. The probe displacement for which local minima of probe force are attained decreases as the moment increases.

Fig. 9d shows the probing map for $M = 1350$ N mm. The probe instabilities appear as early as 0.1 mm of probe displacement and cause a severe truncation of the map. The probing path for the mid-point of the structure exhibits negative probe forces for displacements of 0.075 mm and 0.14 mm, indicating the existence of two adjacent buckled equilibrium states. However, the overarching goal of the probing method is to compute the minimum energy input needed to trigger early buckling for every probe locations, it is not yet possible due to the probe instabilities. At the locations where the probing sequence suddenly stops it is impossible to draw any conclusions regarding the structure's meta-stability. It is therefore necessary to resolve probing sequences past these instabilities, and this is the subject of Section 5.

An important observation is that meta-stability appears earlier for this type of probing than for the double inward probing scheme. For higher moment magnitudes, the minimum of probe force is still achieved at the mid-point of the structure, with regions of negative probe force spreading over a larger portion of the structure. Therefore, there exist multiple locations at which buckled equilibrium states are found. This supports the observations of Section 3 where we saw that localization for the second mode imperfection can occur at multiple locations. However, we see qualitatively that the hill of probe force separating the unbuckled and buckled states is lowest at the mid-point, which signifies that the minimum energy input required to form an inward buckle is also achieved in the middle of each longeron.

4.4. Outward and alternate probing schemes

For the double outward probing scheme it is found that there is no value of the moment for which the probe forces decreases to 0 N. Instead, as the longeron is locally displaced outwards under constant applied moments, the probe force always increases monotonically. Typically, the probe force reaches 1 N for a probe displacement of about 1 mm, which is an order of magnitude higher than the probe force obtained with the double inward probing scheme. Probing does not reveal any buckled equilibria in this case.

The alternate probing scheme involves an inward probe on longeron 1 and an outward probe on longeron 2. The outward probe force increases monotonically, as this case is similar to the double outward probing scheme. However the inward probe force in the center becomes negative for all probe displacements, above a certain moment magnitude. Although the disturbance introduced by probing can be transferred between longerons, the outward probe force never falls to 0 N and hence no buckled equilibria are found.

Similar behavior is observed for the single inward probing scheme. When the outward probe displacement is increased, the probe force monotonically increases, while an inward buckle forms in the unprobed longeron. Similarly to the alternate probing scheme, no equilibrium configurations are encountered, but the probing path is truncated before the prescribed end displacement is reached, due to instabilities. These instabilities are analyzed in Section 5 and it is shown that buckled equilibria exist if probing is extended past instabilities.

4.5. Critical probe work and initial comparison of probing schemes

In order to find the critical buckling mechanism for the strip structure, the probing schemes presented above need to be compared. The critical buckling mechanism corresponds to the minimum amount of energy needed to reach buckled equilibria, but special care has to be taken when computing the energy barrier to buckling and the critical probe work.

In previous buckling and probing studies, the energy barrier refers to the difference in total potential energy between the unbuckled state and the unstable buckled state. As explained in the introduction, the unstable buckled state corresponds to a saddle point (also called mountain pass point) in the energy landscape and is attained for a critical value of the probe displacement, when the zero threshold in probe force is reached. If the main loading is kept constant, the probe work reaches a local maximum at this critical displacement. We will use the terminology "critical probe work" to refer to this local maximum of the probe work. When the probe displacement is monotonic during probing (i.e., no folding of the path), and for a displacement-controlled main loading, the critical probe work is equal to the energy barrier. This scenario is for instance encountered for the probed cylinder under constant end shortening (Virot et al., 2017). However in the present study, the energy barrier and the critical probe work can be different for two reasons:

- Moment-controlled loading implies that probing occurs under a constant value of the end-moment. During probing, the ends of the strip rotate and hence the end-moments do work. As a result, the energy barrier is greater than the critical probe work since it accounts for the end-moments' additional contribution to the energy of the system. However, the constant moments are part of the known conditions the structure is subjected to during operation and, since the contribution of an unknown disturbance is only represented by the probe, the quantity of interest is the critical probe work. The study has been repeated for a rotation-controlled loading and the results are presented in Appendix. In the latter case, the probe work only contributes to the total external work of the system.

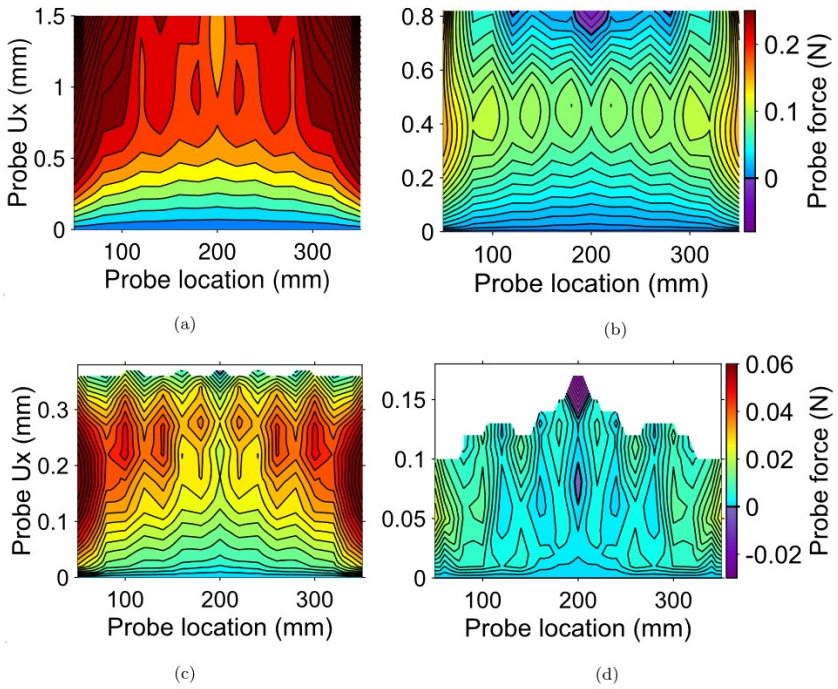

Fig. 9. Single inward probing maps for (a) $M = 800$ N mm, (b) $M = 1040$, (c) $M = 1200$ N mm, and (d) $M = 1350$ N mm. The spacing between contours is 0.02 N for (a) and (b), and 0.005 N for (c) and (d).

- For unstable probing sequences, a vertical tangent can be reached, beyond which the probing path can fold. In such cases, snap-buckling can be triggered before the zero probe force threshold is attained, and the value of the critical probe work is computed at the point of vertical tangent rather than at the first buckled equilibrium. Such cases are presented and analyzed further in Section 5.

Next, the critical probe work for the two inward probing schemes is discussed. Since the probing path does not exhibit any instabilities in the middle of the structure, for both schemes, the critical probe work required to reach the buckled equilibrium states can be computed. The critical probe work obtained for a central probe location and for both probing schemes is shown in Fig. 10.

The single inward probing scheme gives a lower critical probe work than the double inward probing scheme for the entire range of moments considered. As a result, if buckling is triggered early, it will likely consist of a single buckle in the middle of one of the longerons rather than in both longerons. When comparing the local maximum of probe force obtained for both probing schemes, we also see that it is lowest for the single inward probing scheme, regardless of the probe location. It seems therefore that if meta-stability is detected at a specific probe location, the single inward probing scheme would also give the lowest critical probe work at this specific location.

Finally, it has been shown in this section that buckled equilibrium states appear for lower values of moments for the single inward probing scheme. As snaking appears to play a prominent role for this structure, we would expect a sequential formation of single buckles which supports the energy comparison between the two probing schemes. For all of these reasons, the rest of the paper will focus only on the single inward/outward probing schemes.

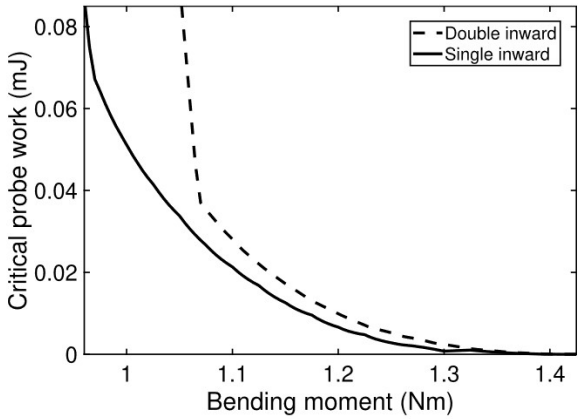

Fig. 10. Critical probe work as a function of the applied bending moment, for both single and double inward probing schemes. It is smallest for the single inward probing scheme.

5. Unstable probing sequences

5.1. Single inward probing

This section extends the probing simulations to cases in which instabilities are encountered. The probing displacement is applied similarly to the previous part of the study, but an arc-length solver (Riks solver) is now used, which allows probing to continue after a vertical tangency (fold) in the probe force vs. probe displacement plane has been reached. Additional probing sequences are computed for the single inward probing scheme and for all probing locations, and the two main types of path instabilities encountered are analyzed.

The results of the analysis for a probe located at 100 mm from the end of the structure are shown in Fig. 11. For $M < 1050$ N mm, the probing path is stable and the probe force exhibits a local maximum and local minimum. However, the probe force is always positive and no locally buckled equilibrium solutions exist. For $M = 1050$ N mm, a vertical tangent is encountered and the path folds. The path eventually restabilizes for a value of probe force of about −0.1 N. However, the restabilized path is short and does not reach positive probe forces. This suggests that another bifurcation is encountered for a probe displacement of about 0.2 mm. This behavior is also encountered for higher values of moments, although the corresponding probing paths do not

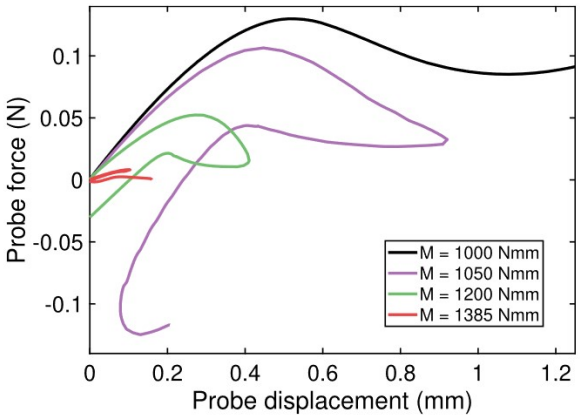

Fig. 11. Probe force vs. probe displacement for a probe located at $z = 100$ mm and for four values of applied moment. The loop formed by the folded path becomes smaller as the moment magnitude increases until it folds on itself for $M = 1385$ N mm.

restabilize for positive values of probe displacement. Fig. 12a shows the probing path for $M = 1050$ N mm with four points 1–4 marking key stages of the probing sequence.

The deformed shapes corresponding to these four points are shown in Fig. 12b. On the stable part of the path (before reaching point 2), displacing the probe results in an increase of the local buckle amplitude. After point 2, the probing path becomes unstable. As the probe displacement decreases, the probe force increases until it reaches point 3 and then decreases to 0 N at point 4, which corresponds to a buckled equilibrium solution. This unstable path corresponds to the change of location of the buckle formed during the stable part of the path. At point 4, the structure is in a buckled equilibrium configuration, but the final buckle location does not correspond to the probing location.

Note that the probe force vs. probe displacement curve has a positive slope at point 4 which means that the equilibrium is stable. The critical probe work required to reach the localized buckled configuration at point 4 corresponds to the shaded area in Fig. 12a. It is important to point out that this area does not correspond to the energy barrier, as explained in Section 4.5. In order to compute the energy barrier, i.e. the difference in total potential energy between the unbuckled state and the buckled state at point 4, the area enclosed by the probing path would have to be considered. The area under the curve formed by points 2, 3 and 4 would have to be subtracted from the shaded area, and the work done by the end-moments would have to be added.

Path folding has also been encountered in compressed spherical shells probed at the apex, under rigid volume control (Thompson and Sieber, 2016), and all of the bifurcations that can arise and disrupt a probing sequence have been described (Thompson et al., 2017). Two approaches have been proposed to explore experimentally these unstable probing sequences. The first one consists in introducing feedback control (Thompson et al., 2017). If the probe displacement and probe force are chosen as inputs, it is then possible to resolve vertical tangents. It is also possible to navigate around the fold and avoid unstable probing paths by using the moment and probe displacement as inputs. Another approach consists in using additional probes to suppress instabilities (Thompson and Sieber, 2016).

Next, the probing paths for a probe located at 160 mm from the end of the structure are shown in Fig. 13. For $M = 1000$ N mm, the path exhibits a local maximum and a local minimum without reaching the zero threshold for the probe force. The path is well behaved and can be resolved with a Newton–Raphson solver. For $M = 1050$ N mm, the probe path reaches a point of vertical tangency for a probe displacement 0.85 mm. The restabilized path extends further and reaches positive probe forces, which indicates the existence of a stable equilibrium solution.

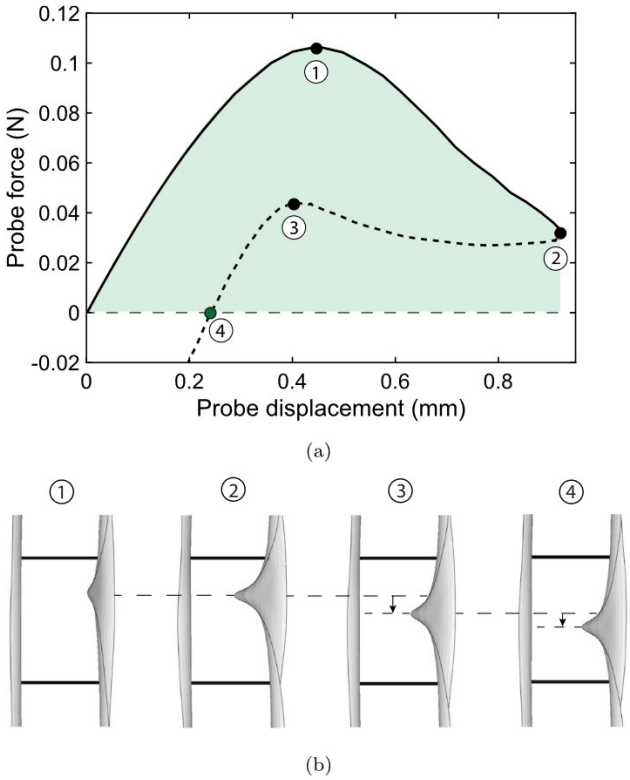

Fig. 12. (a) Probe force vs. displacement for probe at $z = 100$ mm and $M = 1050$ N mm. Four key points are highlighted and correspond to the deformed shapes shown in (b). The solid and dashed lines correspond respectively to the stable and unstable probe characteristic under displacement control. The shaded area is the probe work needed to trigger snap-buckling. (b) Mode shapes obtained at points 1, 2, 3, and 4 on the probing sequence. The stable part of the path (point 1 and 2) corresponds to the growth of the buckle formed by the probe. On the unstable part of the path (points 3 and 4), the previously formed buckle shifts location. Deformations have been magnified by a factor 20.

As the moments increases in magnitude, the path folding is replaced by path spiraling, which indicates that multiple equilibrium solutions exist. The number of equilibrium solutions encountered on the probing path increases as the moment increases. For $M = 1200$ N mm, four equilibrium solutions are detected and for $M = 1300$ N mm the spiraling evolves to reveal five equilibrium solutions. Close to the buckling load, at $M = 1385$ N mm, a single path is observed for extremely small values of probe displacement, which indicates an extremely low critical probe work.

The probing path for $M = 1300$ N mm is shown in Fig. 14a, with four equilibrium states labeled 1–5. The deformed shapes obtained at these points are shown in Fig. 14b. As the probe displacement increases, initially the probe force increases and then decreases. The probing path becomes unstable right before reaching the first equilibrium state (labeled 1). At this point, a buckle in stable equilibrium (buckle 1) is formed in the longeron at the probe location. The unstable path between states 1 and 2 exhibits negative probe forces, and the initially formed buckle travels along the longeron's top edge. This situation is similar to the 100 mm probe location, but the main difference is that the path restabilizes with a sudden increase in probe force. Point 2 is now also an equilibrium state, whereas previously only one equilibrium solution was found. Equilibrium state 2 is also stable. From state 2 to state 3, the probe force increases, and the magnitude of the maximum probe force is about twice the one attained before state 1. On this part of the path, buckle 1 continues to travel along the longeron, and a second buckle (buckle 2) forms at the probe location. The path loses stability at a probe displacement of about 0.4 mm and reaches the

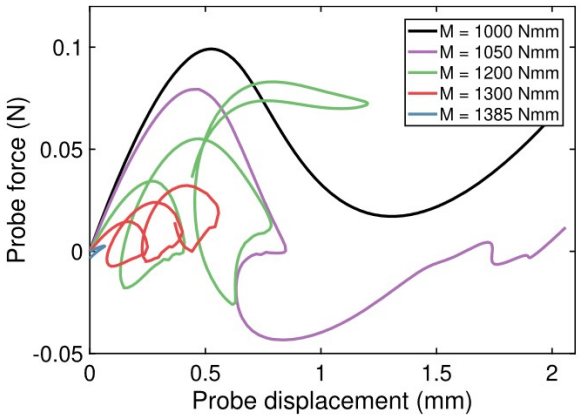

Fig. 13. Probe force vs. displacement for probe at 160 mm and for five values of applied moment.

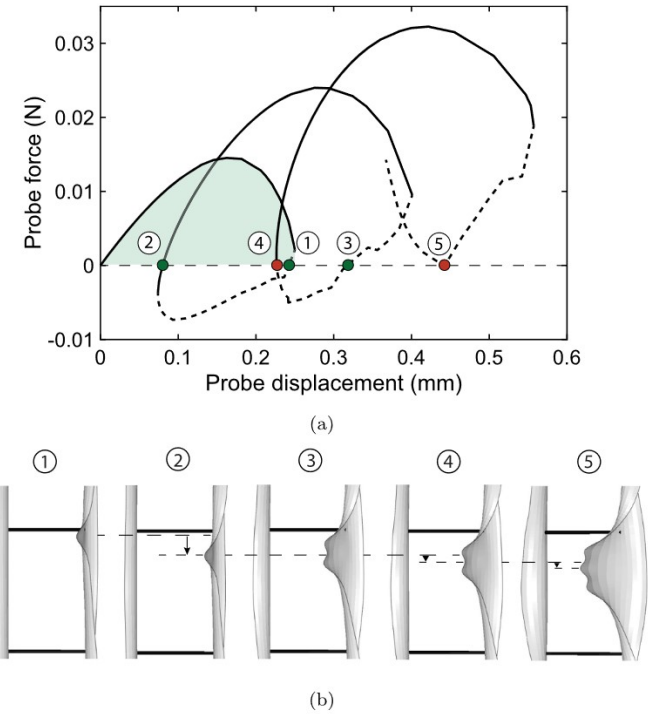

Fig. 14. (a) Probe force vs. displacement for a probe located at $z = 160$ mm and for a moment of $M = 1300$ N mm. The five points highlighted correspond to the deformed shapes shown in (b), magnified by a factor of 40. The solid and dashed lines correspond respectively to the stable and unstable probe characteristic under displacement control. The stable and unstable equilibrium configurations are indicated by green and red dots, respectively.

stable equilibrium 3, for which buckle 1 and buckle 2 are sustained, forming a "train" of 2 buckles. This buckle formation shifts location before reaching the unstable equilibrium 4. The path proceeds with a third loop and the 2-buckle formation continues traveling, while a third buckle (buckle 3) is formed at the probe location. The path reaches equilibrium 5 for which 3 buckles in series are sustained in the longeron. Note that point 5 also corresponds to a local minimum of probe force and as a result, no more negative probe forces appear on the path.

Two other interesting behaviors are observed. First, closer to the strip ends (probe location between 20 mm and 60 mm) some hysteresis is found. The probe displacement and probe force first increase, until reaching a limit point, after which the probe displacement decreases and the path returns to the origin. However, the return path lies below the original, stable path, indicating lower probe forces. Physically, this indicates an interaction between the longerons: the inward displacement imposed on longeron 1 by the probe causes a macroscopic in-plane bending of the full structure, causing the unprobed longeron (longeron 2) to buckle. A similar transfer of disturbance between longerons, through the battens, was also encountered for the alternate probing scheme. Secondly, for some combination of probe locations and moments, the solver stops before the end of the analysis and the full probing path cannot be resolved. This is due to the presence of secondary bifurcations, and therefore the loss of a unique equilibrium path. While path folding and spiraling could be resolved using the Riks solver alone, continuing these probing paths after the bifurcation would require an imperfection to be added in the initial geometry, or more sophisticated continuation algorithms (Groh et al., 2018), which is beyond the scope of this paper. In most cases, path folding is observed before reaching the bifurcation point, but the path stops before reaching the zero threshold for the probe force. Therefore, no equilibrium solutions can be detected. However, it is still possible to compute the probe work required to trigger snap-buckling, when the vertical tangent is reached.

5.2. Single outward probing

No buckled equilibrium solutions were detected when the single outward probing scheme was used in Section 4, and the probe force increased monotonically as the probe displacement increased. Even if buckled equilibrium states seemed unlikely for this type of probing, the probing paths had been prematurely terminated by instabilities and therefore no final conclusion could be reached regarding their existence. Here, the Riks solver is used to compute the probing paths past vertical tangents. Surprisingly, it was found that the single outward probing scheme is able to trigger inward buckled equilibria, and the two main buckling mechanisms are analyzed below.

The first buckling mechanism involves the formation of a buckle in the unprobed longeron. Probing at a location $z = 180$ mm under a moment of $M = 1100$ N mm triggers this behavior, and the corresponding probe force vs. probe displacement curve is shown in Fig. 15a. The structure's deformed shapes obtained at selected points on the path are shown in Fig. 15b. The probing sequence starts with a monotonic increase in probe force as the probe on longeron 1 is displaced outwards. The deformed shape at point 1 shows the large displacement of the probed longeron but no localization is observed. However pulling on longeron 1 results in a global in-plane bending of the structure, which results in an inward displacement of the unprobed longeron 2, since the two longerons are connected by the battens. Past point 1, the probe displacement decreases and the inward displacement of longeron 2 localizes to form a buckle. At point 2, the inward buckle on the unprobed longeron 2 is in equilibrium and stable. Once the probe displacement becomes negative, the single inward probing scheme is recovered and an inward buckle is formed on the probed longeron 1. Path folding is then observed which physically corresponds to the buckle on longeron 1 moving along the longeron, as described in the previous subsection. The only difference here is that the initial outward probing results in an additional inward buckle on longeron 2.

The second buckling mechanism is rather unexpected, as it corresponds to the formation of an inward buckle in the longeron probed outwards. Probing under a moment $M = 1300$ N mm and at a location of 120 mm leads to this behavior. The corresponding probe force vs. probe displacement curve is shown in Fig. 16a and the structure's deformed shapes at key points of the path are shown in Fig. 16b. The probing sequence starts again with a monotonic increase in probe force as the probe on longeron 1 is displaced outwards. The deformed shape at point 1 shows the large displacement of the probed longeron,

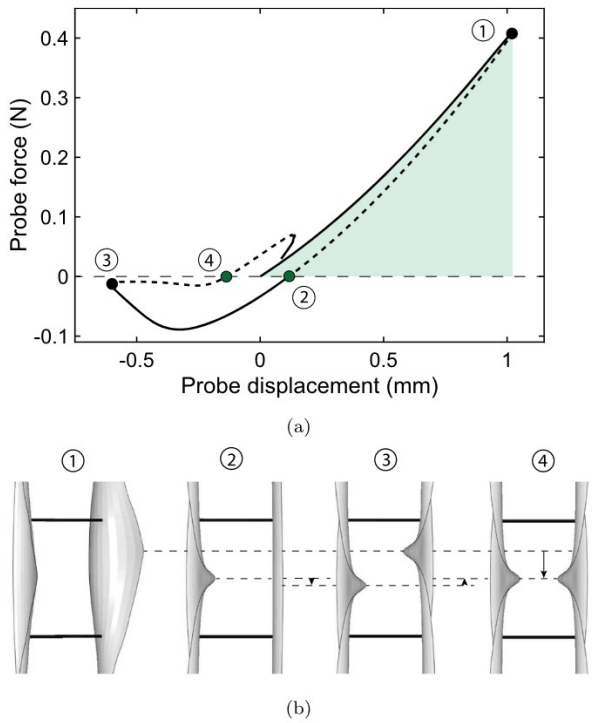

Fig. 15. (a) Probe force vs. displacement for probe at $z = 180$ mm and $M = 1100$ N mm. (b) Deformed shapes corresponding to points 1, 2, 3, and 4, magnified by a factor of 30. The solid and dashed lines correspond respectively to the stable and unstable probe characteristic under displacement control. The stable equilibrium configurations are indicated by green dots.

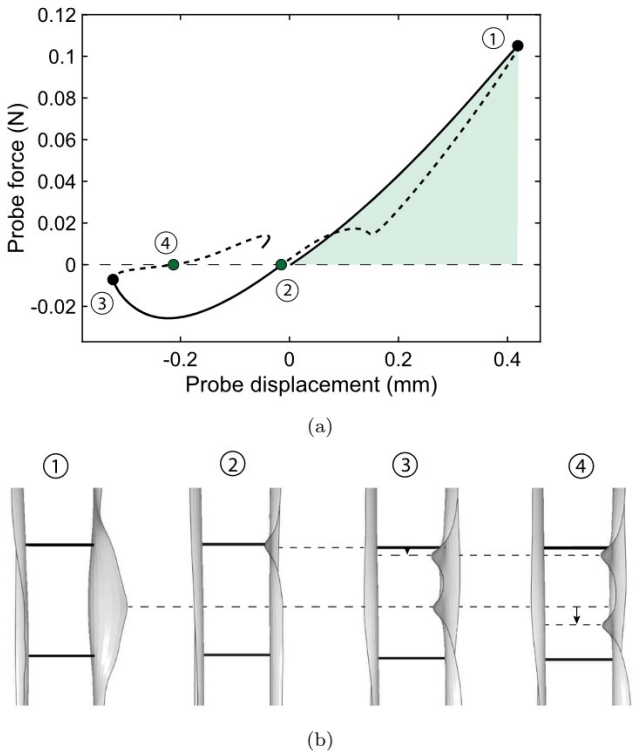

Fig. 16. (a) Probe force vs. displacement for probe at $z = 120$ mm and $M = 1300$ N mm. The four points highlighted correspond to the deformed shape shown in (b), magnified by a factor of 50. The solid and dashed lines correspond respectively to the stable and unstable probe characteristic under displacement control. The stable equilibrium configurations are indicated by green dots.

but inward localization is observed farther away from the probe, on the same longeron. Past point 1, the path becomes unstable and the localized fold present at point 1 corresponds to an inward buckle on the probed longeron. The local hump in probe force observed on the unstable path corresponds to the buckle traveling until the stable equilibrium at point 2 is reached. After point 2, the single inward probing scheme is recovered and an additional buckle is formed on the probed longeron. Path folding is again observed in this case.

Finally, other types of outward probing paths are encountered for different probe locations and consist of a superposition of the two simple buckling sequences described above. Note that once the first buckle has been formed by the outward probing scheme, these paths can exhibit spiraling and lead to a complex series of buckles in equilibrium. An analysis of these complex situations corresponding to even more equilibrium solutions is beyond the scope of this paper.

The main take away is that both the single inward and single outward probing schemes can trigger inward buckling, and no outward buckling has been observed in either case.

5.3. Critical probe work map

Repeating the analysis described above for all probe locations and moments, and for both the single inward and single outward probing schemes, leads to the two critical probe work plots shown in Fig. 17. Each color corresponds to a specific moment magnitude. Dots denote the first zero threshold in probe force, corresponding to a buckled equilibrium. In some cases, secondary bifurcations are encountered on the probing path before reaching the zero probe force threshold. In this case, additional techniques would need to be used to trace the full probing path, however, the critical probe work has been computed and reported without a dot. If the probing path can be fully resolved but never crosses the zero probe force threshold, the maximum work done by the probe is also reported without a dot. Since the problem is symmetric with respect to the middle transverse axis of the strip, only results for half a strip have been presented in Fig. 17. No early buckling can be triggered for probes between $z = 0$ mm and $z = 20$ mm, and hence this region is not shown. Finally, it is important to highlight that the probe location does not necessarily coincide with the buckling location.

The critical probe work for the inward probing scheme is shown in Fig. 17a. Multi-stability is first detected for probing at the midpoint and for $M = 950$ N mm. For higher values of the moment, the meta-stable region extends to almost the entire length of the strip. For moments lower than 1385 N mm, the minimum critical probe work is always reached for probing at 200 mm. For $M = 1000$ N mm, it is about 0.06 mJ and drops to less than 10^{-3} mJ for $M = 1350$ N mm. These magnitudes make early buckling extremely likely to occur. Closer to the first buckling moment ($M = 1400.3$ N mm), the location of the minimum critical probe work changes. It is attained for a probe at 180 mm for $M = 1385$ N mm and shifts to 160 mm for higher values of moments. Note that for this range of high moments, the critical probe work drops to practically zero. At $M = 1400$ N mm, the critical probe work first drops to effectively zero (marked as 10^{-7} in Fig. 17).

The critical probe work for the single outward probing scheme is shown in Fig. 17b. Qualitatively, it resembles the single inward probing, however the critical probe work is consistently higher for this type of probing, indicating that inward probing is the critical disturbance for the strip structure. For $M > 1385$ N mm, the minimum critical probe work is similar for inward and outward probing. At $M = 1400$ N mm, the critical work first drops to zero (marked as 10^{-7} in Fig. 17) but for a probe location of 60 mm, which differs from the single inward probing scheme.

For both probing schemes and for $M < 1385$ N mm (99% of the buckling moment), the minimum critical probe work occurs for probing in the middle of the structure and is extremely low. It can be concluded

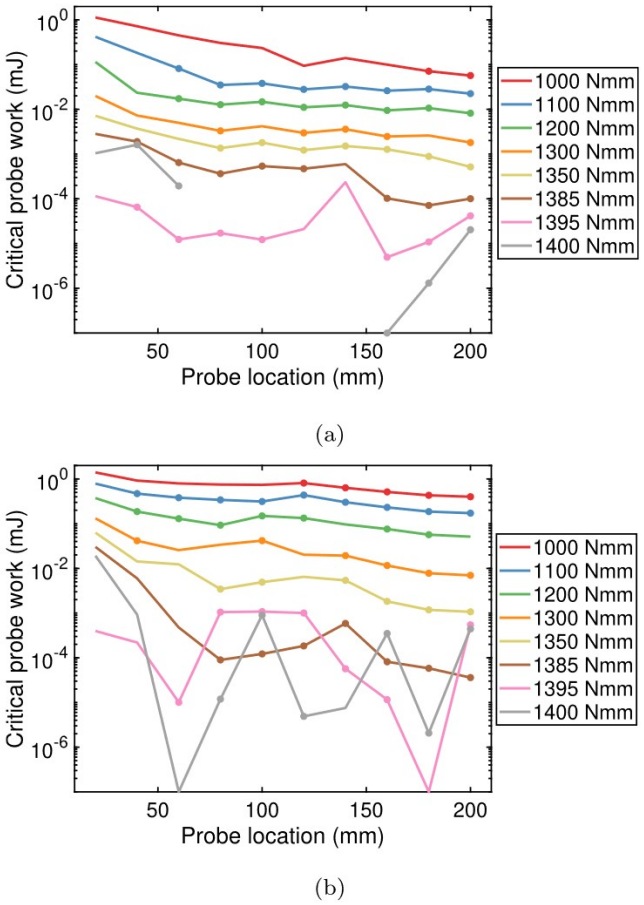

Fig. 17. Critical probe work map for (a) single inward and (b) single outward probing scheme. Dots denote solutions corresponding to the first zero value of the probe force, corresponding to a buckled equilibrium. These plots show similar trends, except that the single outward probing scheme requires more energy to trigger inward buckles.

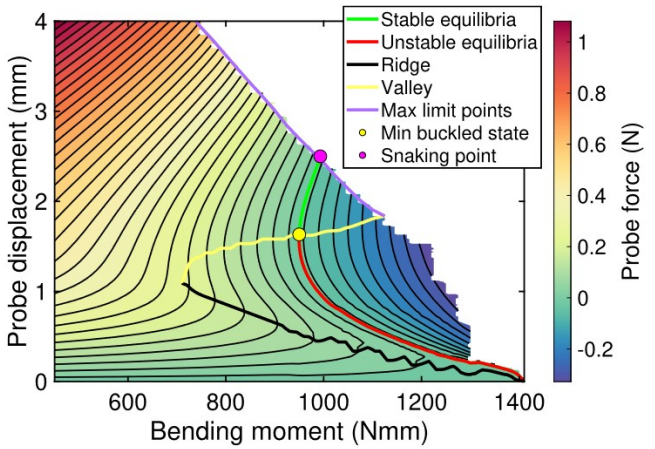

Fig. 18. Stability landscape for the strip critical buckling mechanism (single inward buckling in the middle), showing a region of negative probe force enclosed by a stable/unstable buckled equilibrium contour, separated from the fundamental path by a ridge of probe force. No buckles can be sustained in the structure for moments below the minimal buckling moment ($M = 950$ N mm).

that early buckling is most likely triggered by inward probing in the middle of the structure, and it is thus the critical disturbance. For this specific case, the probing and buckling locations are the same and, therefore, the critical buckling mechanism consists of a localized single buckle in the middle of a longeron.

Finally, rotation-controlled simulations have also been carried out. The corresponding critical probe work maps are presented in Appendix.

6. Stability landscape for critical localized buckling

The notion of a stability landscape of shell buckling was introduced (Virot et al., 2017) as a way to characterize the meta-stable nature of cylindrical thin-shell buckling. The experiments in this original study used soda cans, and a local radial displacement was imposed in the middle of the compressed can using a small ball probe (called a "poker" in Virot et al. (2017)).

The stability landscape is the surface created when the probe force is plotted as a function of the probe displacement for various levels of the main loading parameter (axial compression or end-shortening of the cylinder). The landscape provides a very useful way to quantify the impact of probing on the buckling behavior and a general way to study the structure's buckling sensitivity to disturbances. In the cylinder case, the probe location coincides with the location of the critical buckling mechanism, which corresponds to the formation of a single dimple in the middle of the cylinder. Hence, in this case the probing experiment is aimed at triggering this specific mode (lowest mountain pass point).

In the previous section, the critical buckling mechanism for the strip structure was identified. It was established that local buckling can first appear as a single inward buckle forming in the middle of one longeron. As a result the critical stability landscape of shell buckling for this new structure has been constructed and is presented in Fig. 18.

This landscape matches qualitatively the landscape for the compressed cylindrical shell, as well as the stability landscape for more structural complex geometries and loading (Royer and Pellegrino, 2020). Several important features are observed (Virot et al., 2017) and are explained here. The point of spontaneous buckling corresponds to the state for which the structure will undergo buckling without any action from the probe. This point is reached when the moment attains the buckling load (accounting for nonlinear pre-buckling deformation). However, before reaching this point, buckled equilibrium solutions are accessible through probing. These solutions correspond to the contour for which the probe force is zero (for a non-zero probe displacement). It consists of two parts: stable and unstable. For a specific value of the moment, corresponding to the lowest value of moment for which a buckled equilibrium solution exists, the stable and unstable states coincide. This condition represents the onset of meta-stability and the associated state is called the minimally buckled state (Virot et al., 2017). This moment value is denoted as the minimal buckling moment.

For the strip structure, the minimal buckling moment is 950 N mm (68% of the buckling moment), and the probe displacement at the minimally buckled state is 1.6 mm. Below the minimal buckling moment, no local buckles can be sustained in the structure. This load may serve as an effective lower bound for experimental buckling loads (Groh and Pirrera, 2019).

During a moment-controlled experimental probing sequence, where the probe is not attached to the structure, the longeron flange will dynamically snap as soon as the probe reaches past the unstable equilibrium contour, since the probe will experience negative reaction forces. Depending on the moment at which probing is carried out, the structure can restabilize and reach the stable equilibrium contour. For a moment above a critical value, corresponding to the snaking point of Fig. 18, the structure will not restabilize and may completely collapse. The snaking moment is $M = 993$ N mm (71% of the buckling moment). It is possible to probe the stable post-buckling path and compute the critical probe work required for early snaking, following the same methodology.

It is important to realize that the existence of the stable equilibrium contour is not guaranteed. It depends on the particular structure under study, and also on whether the experiment/simulation is load controlled or displacement controlled. For example, a spherical shell under

external pressure will exhibit stable buckled states when loaded under volume-control but has no stable buckled states (other than complete collapse) under pressure-control (Hutchinson and Thompson, 2017a). For the SSPP strip structures described in the Introduction, it has been observed that the stable buckled equilibrium contour can extend much farther than the first buckling load (Royer and Pellegrino, 2020).

The local maxima of probe force define the ridge of the stability landscape, and form a hill of energy between the fundamental path and the unstable buckled equilibrium states. At any applied moment, the critical probe work is the minimum energy that must be input into the structure for it to locally buckle. This quantity is directly related to the buckling sensitivity to disturbances, referred to as "shock-sensitivity" (Thompson and van der Heijden, 2014). The ridge meets the fundamental path at the point of spontaneous buckling under prescribed probe force (but not under prescribed probe displacement). Past this point, negative probe forces are encountered as soon as the probe is displaced. The local minima of probe force form the valley of the stability landscape, defining the limit beyond which probing paths restabilize. The valley intersects with the buckled equilibrium contour at the minimally buckled state after which the minimum probe force becomes negative.

The ridge and valley intersect at $M = 710$ N mm (51% of the non-linear buckling moment), after which the landscape starts exhibiting a negative probing stiffness. For higher values of probe displacements, the stability landscape is bounded by limit points ending each probing sequence. The ridge, valley, and maximum limit points form the landscape's foldline which defines more generally the range of stability for the structure against the single buckle mode of deformation. Snaking, which corresponds to secondary modes being triggered, will occur when the maximum limit points are exceeded.

Finally, rotation-controlled simulations have been carried out and yield qualitatively the same landscape. The rotation-controlled stability landscape is shown in Appendix.

7. Conclusion

This paper has presented a numerical investigation of the buckling sensitivity of a complex thin-shell strip structure, applying the novel probing methodology previously used for cylindrical and spherical shells. The focus has been on a single geometry, inspired by novel designs for spacecraft structures, with the goal of paving the way for experimental studies (Royer, 2021).

First, a classical post-buckling analysis has been conducted, which consisted in seeding imperfections based on the structure's buckling modes in the initial geometry. This analysis has shown multiple localized post-buckling solutions originating from a limited set of nine buckling modes, and providing evidence that the structure exhibits spatial chaos.

The probing methodology is well suited to finding the critical buckling mechanism. By probing along the entire structure, it has been found that only localized buckling in the inward direction can be triggered before the buckling moment is reached. Furthermore, a comparison between single and double inward probing schemes highlighted that the longerons will most likely not undergo buckling simultaneously and will rather exhibit a sequential formation of buckles known as snaking, which was also supported by the classical post-buckling analysis. However, when probing is not done in the middle of the structure, unstable probing sequences were observed and, therefore, an arc-length solver was used. This refined analysis highlighted complex behaviors such as buckles traveling along the structure and multiple equilibrium paths juxtaposed next to each other. It has been shown that unstable outward probing can lead to local inward buckling through an interaction between structural components.

A particular feature of the equilibrium paths obtained in the present study, which had not been reported before, is the formation of spiral paths that indicate the existence of multiple equilibrium configurations.

This generalized probing approach has enabled the construction of a critical probe work map from which we concluded that a single inward buckle forming on a single longeron is the buckling mechanism requiring the least amount of disturbance to be triggered before reaching the buckling moment. An in depth study of the critical buckling mode has enabled the construction of a stability landscape of shell buckling. It highlights the region of stability for the buckled structure as well as the region for which restabilization occurs, between the minimal buckling moment and the snaking moment. This stability landscape is qualitatively similar to previous, experimentally based, landscapes for cylindrical shells.

Although the core of the paper has presented results for moment-controlled loading, for which probing occurs under a constant moment, rotation-controlled loading has also been studied. It leads to the same qualitative results for this structure, as shown in Appendix.

More generally, it has been shown that the probing methodology can be applied to more complex structures than cylindrical and spherical shells. Therefore, the use of such a technique for complex assemblies of thin-shell components seems to be possible and could enable an in-depth understanding of any structure's buckling sensitivity. One could think about designing for a specific level of disturbance during operations and thus push the structure's capabilities to its fullest. If one does not have a full knowledge of potential disturbances, an experimental determination of the minimal buckling load seems to provide an excellent buckling criterion. However, more work needs to be done to assess how initial imperfections erode the critical probe work required to trigger buckling and how they could provide connections between the adjacent post-buckling path and the fundamental path. Recent studies have suggested that the minimal buckling load varies rather slowly for imperfections of limited amplitude (about 50% of the shell thickness) (Royer and Pellegrino, 2020), whereas the critical probe work is significantly affected. A detailed investigation of the role of imperfections on the buckling sensitivity will be the subject of a future paper.

Declaration of competing interest

The authors declare that they have no known competing financial interests or personal relationships that could have appeared to influence the work reported in this paper.

Acknowledgments

FR and SP gratefully acknowledge financial support from the Space Solar Power Project at Caltech.

Appendix. Rotation-controlled study

The analysis presented in the paper has been repeated for rotation-controlled main loading. Here the rotation is prescribed at the two ends of the strips, at the reference points shown in Fig. 2. The moment-controlled and rotation-controlled studies lead to the same qualitative results. The same buckling modes and unstable probing paths are observed, and the critical probe work maps can be computed. These maps are shown in Fig. A.19a for the single inward probing scheme and in Fig. A.19b for the single outward probing scheme. The values of applied rotations are chosen such that they correspond one-to-one to the moment magnitudes in Fig. 17, on the structure's fundamental path.

One important difference here is that the probe work accounts for all of the external work, since the end moments are not doing any work. For rotations (or corresponding moments) between 0.745 deg and 0.894 deg, a higher critical probe work is required to trigger snap-buckling when the loading is rotation-controlled rather than moment-controlled. In this initial range of rotations, the minimum critical probe work is still achieved by probing in the center ($z =$

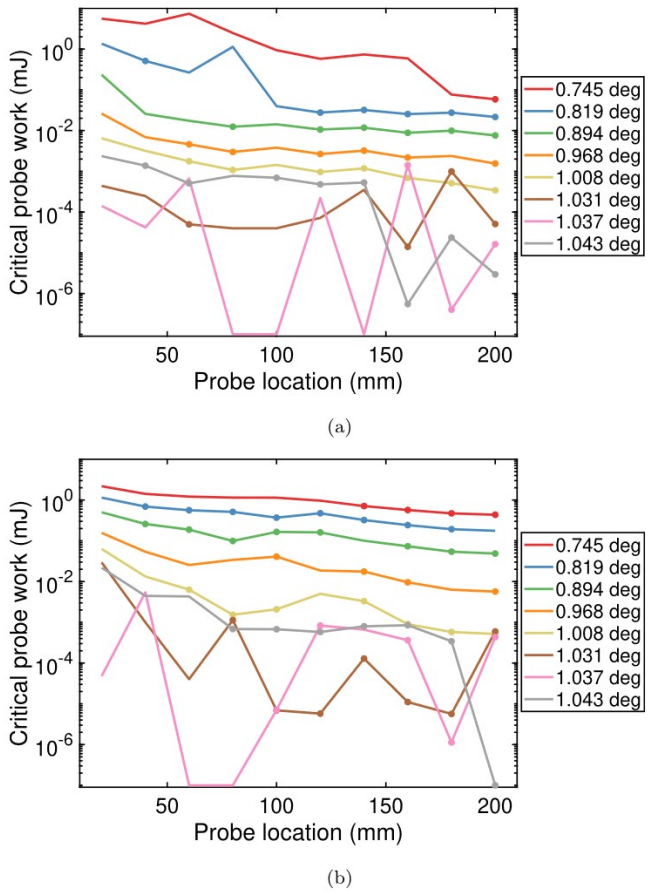

Fig. A.19. (a) Critical probe work map for single inward probing scheme. Dots denote solutions corresponding to the first zero value of the probe force, corresponding to a buckled equilibrium. (b) Critical probe work map for single outward probing scheme.

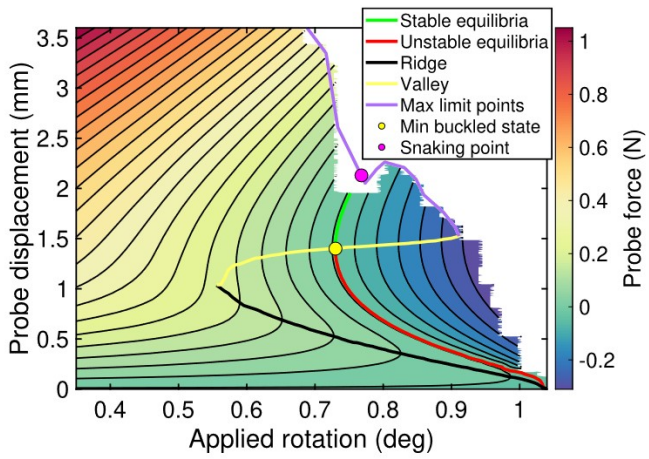

Fig. A.20. Stability landscape for critical buckling mechanism (single inward buckling in the middle) and for rotation-controlled loading.

200 mm), and therefore the single inward buckling in the middle of one longeron is also the critical buckling mechanism for a rotation-controlled loading. For higher values of rotation, the critical probe work is higher for the moment-controlled case, even if it has a similar order of magnitude for both types of loading. Closer to the buckling point, we observe that the critical probe work becomes chaotic across the structure's length.

For the critical buckling mechanism identified above (single inward buckle at $z = 200$ mm), the rotation-controlled stability landscape can be built and is shown in Fig. A.20. It presents the same features as the moment-controlled stability landscape. In both studies, the probing path restabilizes after the minimally buckled state. The minimal buckling rotation is about 70% of the classical buckling rotation which is comparable to the minimal buckling moment which was 68% of the classical buckling moment. Probing becomes unstable close to the snaking point which explains the missing area in the map shown in Fig. A.20. It is important to point out that when the applied rotation is held constant, the area under the probe force vs. probe displacement curve is the critical probe work but also the energy barrier between the unbuckled equilibrium and the unstable buckled equilibrium.

References

Abbasi, A., Yan, D., Reis, P.M., 2021. Probing the buckling of pressurized spherical shells. J. Mech. Phys. Solids 155, 104545. http://dx.doi.org/10.1016/j.jmps.2021.104545.

Abramian, A., Virot, E., Lozano, E., Rubinstein, S.M., Schneider, T.M., 2020. Nondestructive prediction of the buckling load of imperfect shells. Phys. Rev. Lett. 125 (22), 225504. http://dx.doi.org/10.1103/PhysRevLett.125.225504.

Arya, M., Lee, N., Pellegrino, S., 2016. Ultralight structures for space solar power satellites. In: 3rd AIAA Spacecraft Structures Conference. http://dx.doi.org/10.2514/6.2016-1950.

Audoly, B., Hutchinson, J.W., 2020. Localization in spherical shell buckling. J. Mech. Phys. Solids 136, 103720. http://dx.doi.org/10.1016/j.jmps.2019.103720.

Donnell, L.H., Wan, C.C., 1950. Effect of imperfections on buckling of thin cylinders and columns under axial compression. J. Appl. Mech. 17, 73–83.

Gdoutos, E., Leclerc, C., Royer, F., Tü, D.A., Pellegrino, S., 2019. Ultralight spacecraft structure prototype. In: AIAA Scitech 2019 Forum. http://dx.doi.org/10.2514/6.2019-1749.

Gdoutos, E., Truong, A., Pedivellano, A., Royer, F., Pellegrino, S., 2020. Ultralight deployable space structure prototype. In: AIAA Scitech 2020 Forum. http://dx.doi.org/10.2514/6.2020-0692.

Gerasimidis, S., Virot, E., Hutchinson, J.W., Rubinstein, S.M., 2018. On establishing buckling knockdowns for imperfection-sensitive shell structures. J. Appl. Mech. 85, http://dx.doi.org/10.1115/1.4040455.

Goel, A., Lee, N., Pellegrino, S., 2017. Trajectory design of formation flying constellation for space-based solar power. In: 2017 IEEE Aerospace Conference. pp. 1–11. http://dx.doi.org/10.1109/AERO.2017.7943711.

Groh, R., Avitabile, D., Pirrera, A., 2018. Generalised path-following for well-behaved nonlinear structures. Comput. Methods Appl. Mech. Engrg. 331, 394–426. http://dx.doi.org/10.1016/j.cma.2017.12.001.

Groh, R.M.J., Pirrera, A., 2019. On the role of localizations in buckling of axially compressed cylinders. Proc. R. Soc. A 475, 20190006. http://dx.doi.org/10.1098/rspa.2019.0006.

Hilburger, M., 2012. Developing the next generation shell buckling design factors and technologies. In: 53rd AIAA/ASME/ASCE/AHS/ASC Structures, Structural Dynamics and Materials Conference. http://dx.doi.org/10.2514/6.2012-1686.

Horák, J., Lord, G.J., Peletier, M.A., 2006. Cylinder buckling: The mountain pass as an organizing center. SIAM J. Appl. Math. 66, 1793–1824. http://dx.doi.org/10.1137/050635778.

Hu, N., Burgueño, R., 2015. Buckling-induced smart applications: recent advances and trends. Smart Mater. Struct. 24, 063001. http://dx.doi.org/10.1088/0964-1726/24/6/063001.

Hunt, G., Neto, E., 1991. Localized buckling in long axially-loaded cylindrical shells. J. Mech. Phys. Solids 39, 881–894. http://dx.doi.org/10.1016/0022-5096(91)90010-L.

Hutchinson, J.W., 2016. Buckling of spherical shells revisited. Proc. R. Soc. A 472, 20160577. http://dx.doi.org/10.1098/rspa.2016.0577.

Hutchinson, J.W., Thompson, J.M.T., 2017a. Nonlinear buckling behaviour of spherical shells: barriers and symmetry-breaking dimples. Phil. Trans. R. Soc. A 375, 20160154. http://dx.doi.org/10.1098/rsta.2016.0154.

Hutchinson, J.W., Thompson, J.M.T., 2017b. Nonlinear buckling interaction for spherical shells subject to pressure and probing forces. J. Appl. Mech. 84, http://dx.doi.org/10.1115/1.4036355.

Koiter, W.T., 1945. On the Stability of Elastic Equilibrium. Amsterdam, Holland, pp. 201–213.

Kreilos, T., Schneider, T.M., 2017. Fully localized post-buckling states of cylindrical shells under axial compression. Proc. R. Soc. A 473, 20170177. http://dx.doi.org/10.1098/rspa.2017.0177.

Leclerc, C., Pellegrino, S., 2020. Nonlinear elastic buckling of ultra-thin coilable booms. Int. J. Solids Struct. 203, 46–56. http://dx.doi.org/10.1016/j.ijsolstr.2020.06.042.

Lee, A., López Jimé, F., Marthelot, J., Hutchinson, J.W., Reis, P.M., 2016. The geometric role of precisely engineered imperfections on the critical buckling load of spherical elastic shells. J. Appl. Mech. 83, http://dx.doi.org/10.1115/1.4034431.

Marthelot, J., López Jimé, F., Lee, A., Hutchinson, J.W., Reis, P.M., 2017. Buckling of a pressurized hemispherical shell subjected to a probing force. J. Appl. Mech. 84, http://dx.doi.org/10.1115/1.4038063.

Medina, E., Farrell, P.E., Bertoldi, K., Rycroft, C.H., 2020. Navigating the landscape of nonlinear mechanical metamaterials for advanced programmability. Phys. Rev. B 101, 064101. http://dx.doi.org/10.1103/PhysRevB.101.064101.

Murphey, T., Banik, J., 2011. Triangular rollable and collapsible boom. U.S. Patent 7, 895, 79.

NASA, 1965. Buckling of thin-walled circular cylinders. In: NASA Space Vehicle Design Criteria, NASA SP-8007. (Revised 1968). Technical Report, NASA.

Rahman, T., Jansen, E., 2010. Finite element based coupled mode initial post-buckling analysis of a composite cylindrical shell. Thin-Walled Struct. 48, 25–32. http://dx.doi.org/10.1016/j.tws.2009.08.003.

Riks, E., 1979. An incremental approach to the solution of snapping and buckling problems. Int. J. Solids Struct. 15, 529–551. http://dx.doi.org/10.1016/0020-7683(79)90081-7.

Royer, F., 2021. Probing the Buckling of Thin-Shell Space Structures (PhD Dissertation). California Institute of Technology, http://dx.doi.org/10.7907/ksn2-t598.

Royer, F., Pellegrino, S., 2020. Buckling of ultralight ladder-type coilable space structures. In: AIAA Scitech 2020 Forum. http://dx.doi.org/10.2514/6.2020-1437.

Royer, F., Pellegrino, S., 2022. Probing the stability of ladder-type coilable space structures. AIAA J. 60 (4), 2000–2012. http://dx.doi.org/10.2514/1.J060820.

Shen, J., Groh, R.M.J., Schenk, M., Pirrera, A., 2021a. Experimental path-following of equilibria using Newton's method, Part I: Theory, modelling, experiments. Int. J. Solids Struct. 210-211, 203–223. http://dx.doi.org/10.1016/j.ijsolstr.2020.11.037.

Shen, J., Groh, R.M.J., Schenk, M., Pirrera, A., 2021b. Experimental path-following of equilibria using Newton's method, Part II: Applications and outlook. Int. J. Solids Struct. 213, 25–40. http://dx.doi.org/10.1016/j.ijsolstr.2020.11.038.

Shen, J., Groh, R.M.J., Wadee, M.A., Schenk, M., Pirrera, A., 2022. Probing the stability landscape of prestressed stayed columns susceptible to mode interaction. Eng. Struct. 251, 113465. http://dx.doi.org/10.1016/j.engstruct.2021.113465.

Thompson, J.M.T., 2015. Advances in shell buckling: Theory and experiments. Int. J. Bifurcation Chaos 25, 1530001. http://dx.doi.org/10.1142/S0218127415300013.

Thompson, J.M.T., van der Heijden, G.H.M., 2014. Quantified shock-sensitivity above the maxwell load. Int. J. Bifurcation Chaos 24, 1430009. http://dx.doi.org/10.1142/S0218127414300092.

Thompson, J.M.T., Hutchinson, J.W., Sieber, J., 2017. Probing shells against buckling: A nondestructive technique for laboratory testing. Int. J. Bifurcation Chaos 27, 1730048. http://dx.doi.org/10.1142/S0218127417300488.

Thompson, J.M.T., Sieber, J., 2016. Shock-sensitivity in shell-like structures: With simulations of spherical shell buckling. Int. J. Bifurcation Chaos 26, 1630003. http://dx.doi.org/10.1142/S0218127416300032.

Thompson, J., Virgin, L., 1988. Spatial chaos and localization phenomena in nonlinear elasticity. Phys. Lett. A 126, 491–496. http://dx.doi.org/10.1016/0375-9601(88)90045-X.

Virot, E., Kreilos, T., Schneider, T.M., Rubinstein, S.M., 2017. Stability landscape of shell buckling. Phys. Rev. Lett. 119, 224101. http://dx.doi.org/10.1103/PhysRevLett.119.224101.

Von Karman, T., Tsien, H.-S., 1941. The buckling of thin cylindrical shells under axial compression. J. Aeronaut. Sci. 8, 303–312. http://dx.doi.org/10.2514/8.10722.

Wadee, M.K., Hunt, G.W., Whiting, A.I.M., 1997. Asymptotic and Rayleigh–Ritz routes to localized buckling solutions in an elastic instability problem. Proc. R. Soc. Lond. Ser. A Math. Phys. Eng. Sci. 453, 2085–2107. http://dx.doi.org/10.1098/rspa.1997.0112.

Yadav, K.K., Cuccia, N.L., Virot, E., Rubinstein, S.S., Gerasimidis, S., 2021. A non-destructive technique for the evaluation of thin cylindrical shells' axial buckling capacity. J. Appl. Mech. 88, 5. http://dx.doi.org/10.1115/1.4049806.

Zareei, A., Deng, B., Bertoldi, K., 2020. Harnessing transition waves to realize deployable structures. Proc. Natl. Acad. Sci. 117, 4015–4020. http://dx.doi.org/10.1073/pnas.1917887117.